Finite-element analysis of controlled-source electromagnetic induction using Coulomb-gauged potentials

Eugene A. Badea*, Mark E. Everett‡, Gregory A. Newman**, and Oszkar Biro§

ABSTRACT

A 3-D finite-element solution has been used to solve controlled-source electromagnetic (EM) induction problems in heterogeneous electrically conducting media. The solution is based on a weak formulation of the governing Maxwell equations using Coulomb-gauged EM potentials. The resulting sparse system of linear algebraic equations is solved efficiently using the quasi-minimal residual method with simple Jacobi scaling as a preconditioner. The main aspects of this work include the implementation of a 3-D cylindrical mesh generator with high-quality local mesh refinement and a formulation in terms of secondary EM potentials that eliminates singularities introduced by the source. These new aspects provide quantitative induction-log interpretation for petroleum exploration applications. Examples are given for 1-D, 2-D, and 3-D problems, and favorable comparisons are presented against other, previously published multidimensional EM induction codes. The method is general and can also be adapted for controlled-source EM modeling in mining, groundwater, and environmental geophysics in addition to fundamental studies of EM induction in heterogeneous media.

INTRODUCTION

The controlled-source electromagnetic method (CSEM) is well established in geophysical prospecting. The CSEM method involves energizing the electrically conducting earth with an inductively coupled or directly coupled time-varying source of current and measuring with coincident or remote receivers the secondary electromagnetic (EM) field caused by the resulting eddy currents. The secondary field, at frequencies where the displacement current is negligible, depends primarily on the electrical conductivity distribution of the ground. In CSEM applications, the transmitters and receivers may be airborne, placed on the surface, or located in a borehole. A good overview of the CSEM method can be found in Nabighian (1988, 1991).

Wireline induction logging is a CSEM application that uses coaxial borehole transmitter and receiver coils of fixed separation. The method has long been used within the oil and gas industry (Doll, 1949) to infer in-situ electrical conductivity depth profiles within reservoirs. The electrical conductivity profiles, especially when analyzed jointly with other physical properties derived from well logs, are important because they can aid in diagnosing the structural, textural, and lithographic variations of the formation. In some cases they can permit an estimation of hydrocarbon potential. An introduction to the theory of induction logging can be found in several references (Moran and Kunz, 1962; Chang and Anderson, 1984; Kaufman and Keller, 1989; van den Berg and van der Horst, 1995).

It is widely believed that CSEM prospecting methodologies, including but not limited to induction logging, will benefit from an improved quantitative understanding of CSEM responses in arbitrary 3-D geological settings. The development of such an understanding hinges on the ability to model EM induction in 3-D electrically conducting media. Several algorithms already exist for determining the EM response of a 3-D conducting earth to CSEM or plane-wave excitation (Wang and Hohmann, 1993; Druskin and Knizhnermann, 1994; Newman and Alumbaugh, 1995; Xiong and Tripp, 1995; Everett and Schultz, 1996; Anderson et al., 1996; Smith, 1996; Avdeev et al., 1997; Zhdanov and Fang, 1997; Zanoubi et al., 1999). The demanding programming and storage requirements of forward modeling, the potential economic and scientific benefits of improvements

in geophysical prospecting methods, and the complexity of the earth's geology all stimulate additional research into techniques for efficient and accurate solutions capable of handling general 3-D electrical conductivity distributions.

Only a short time ago, finite-element (FE) modeling of 3-D EM induction for geophysical prospecting applications was considered beyond the capability of readily available computers. Now it is tractable on desktop workstations. Finite-element methods have enjoyed widespread popularity for some time in engineering computational electromagnetics (Biro and Preis, 1989; Boyse et al., 1992; Mur, 1993) and are presently benefiting from advances in unstructured mesh generation, sparse matrix solvers, postprocessing, and visualization techniques.

We consider an FE algorithm for inductively coupled 3-D CSEM modeling for geophysical prospecting applications. The algorithm is based on the so-called $(\mathbf{A}_s, \Psi_s)$ secondary coupled-potential formulation of Maxwell's equations. Similar formulations but in terms of total EM potentials $(\mathbf{A}, \Psi)$ have been used by Biro and Preis (1989) to solve eddy current problems and by Everett and Schultz (1996) to model global-scale geomagnetic induction in the earth's upper mantle. Our interest and the numerical examples presented here pertain to borehole induction logging, but the algorithm is quite general. For example, it could be applied to surface and airborne CSEM problems.

FINITE-ELEMENT ANALYSIS

FE and finite-difference (FD) methods (Wang and Hohmann, 1993; Newman and Alumbaugh, 1995; Anderson et al., 1996; Smith, 1996) are numerical techniques for solving Maxwell's diffusion equations in inhomogeneous, electrically conducting media. The two methods are comparable in terms of solution accuracy, storage requirements, and execution speed. The FE method operates with completely unstructured meshes whose element boundaries can be made to conform to irregular geometries that are characteristic of subsurface heterogeneities, including the deviating boreholes, fluid invasion zones, and dipping geological formations routinely encountered in petroleum well logging. The FD method operates with structured grids that do not conform to irregular configurations.

Integral equation and series solutions to 3-D CSEM problems in geophysics are also available (Xiong and Tripp, 1995; Avdeev et al., 1997; Zhdanov and Fang, 1997) and are computationally efficient in terms of computer memory and execution speed. For example, Avdeev et al. (1997) use a modified Neumann series approach in which an unknown equivalent source current density drives a secondary EM field. The method is rapidly convergent and efficient compared with traditional integral equation methods where inversion of a full matrix is required.

FE solutions to EM induction problems can be formulated in terms of coupled vector-scalar potentials $(\mathbf{A}, \Psi)$ or directly in terms of an electric or magnetic field vector $\mathbf{E}$ or $\mathbf{H}$. While both formulations offer their own advantages, they must satisfy the following two key requirements: (1) the normal electric field component is permitted to jump at material interfaces while the tangential field components remain continuous and (2) the calculated EM fields contain no purely divergent spurious modes. In an $\mathbf{E}$ or $\mathbf{H}$ field formulation, these requirements can be met with the use of an explicit penalty coefficient on the EM field divergence (Zanoubi et al., 1999) or else by adopting specialized vector or edge elements (Barton and Cendes, 1987; Sugeng,

1998; Zanoubi et al., 1999.) By construction, edge elements are divergence free and hence cannot support spurious modes. The unknowns are the tangential components of the electric field along edges of the elements. Edge elements also permit the normal component of the electric field to be discontinuous across material interfaces.

An alternative to a direct $\mathbf{E}$ or $\mathbf{H}$ field formulation is to use gauged EM potentials (Biro and Preis, 1989.) This approach is taken here. Since the magnetic vector potential $\mathbf{A}$ and electric scalar potential Ψ are both continuous across material interfaces, edge elements are not needed. Furthermore, enforcing the Coulomb gauge condition $\nabla \cdot \mathbf{A} = 0$ ensures that the calculated EM potentials contain no purely divergent spurious modes (Paulsen and Lynch, 1991).

Gauged EM potentials

Electric and magnetic fields at low frequencies (such that displacement currents can be neglected) satisfy the diffusive Maxwell's equations:

$$\nabla \times \mathbf{E} = i\omega\mu_0\mathbf{H}, \tag{1}$$

$$\nabla \times \mathbf{H} = \mathbf{J} = \mathbf{J}_S + \sigma\mathbf{E}, \tag{2}$$

where ω is the angular frequency, μ_0 is the permeability of free space, and $\sigma(\mathbf{r})$ is the spatially varying electrical conductivity of the geological formation being studied. The electric current density $\mathbf{J}$ divides into a source term $\mathbf{J}_S$, which is known, plus an ohmic conduction term $\sigma\mathbf{E}$, which describes the induced or eddy currents inside the earth. The underlying $\exp(-i\omega t)$ time dependence is implicitly assumed in these equations. A constitutive equation $\mathbf{B} = \mu_0\mathbf{H}$ relates the magnetic induction and magnetic field vectors. The divergence-free conditions $\nabla \cdot \mathbf{J} = 0$ and $\nabla \cdot \mathbf{B} = 0$ are also imposed, indicating no point sources or sinks of electric current or magnetic induction exist inside the solution domain Ω.

Equations (1) and (2) sometimes are solved more readily if the EM field $(\mathbf{E}, \mathbf{H})$ is expressed in terms of a magnetic vector potential $\mathbf{A}$ and an electric scalar potential Φ, defined according to the following pair of equations:

$$\mathbf{B} \equiv \nabla \times \mathbf{A}, \tag{3}$$

$$\mathbf{E} \equiv i\omega\mathbf{A} - \nabla\Phi. \tag{4}$$

In terms of the EM potentials, equation (2) becomes the curl–curl equation:

$$\nabla \times \nabla \times \mathbf{A} = \mu_0\mathbf{J}_S + \mu_0\sigma(i\omega\mathbf{A} - \nabla\Phi). \tag{5}$$

The discretized curl–curl equation leads to asymmetric FE matrices and the possibility of numerically unstable spurious modes (see Paulsen and Lynch, 1991.) To avoid these numerical difficulties, we follow the approach of Biro and Preis (1989) and incorporate the term $-\nabla(\nabla \cdot \mathbf{A})$ to the left side of equation (5) to get

$$\nabla \times \nabla \times \mathbf{A} - \nabla(\nabla \cdot \mathbf{A}) - i\omega\mu_0\sigma(\mathbf{A} + \nabla\Psi) = \mu_0\mathbf{J}_S. \tag{6}$$

The added term vanishes and equation (5) remains unchanged as long as the Coulomb gauge condition $\nabla \cdot \mathbf{A} = 0$ is satisfied. Applying the vector identity $\nabla \times \nabla \times \mathbf{A} - \nabla(\nabla \cdot \mathbf{A}) = -\nabla^2\mathbf{A}$ shows that equation (6) is equivalent to a vector Helmholtz equation

$$\nabla^2\mathbf{A} + i\omega\mu_0\sigma(\mathbf{A} + \nabla\Psi) = -\mu_0\mathbf{J}_S, \tag{7}$$

for which the discretized form is numerically very stable. In deriving equations (6) and (7) we have introduced the reduced scalar potential $\Phi \equiv -i\omega\Psi$, which will lead to a symmetric FE matrix.

By taking the divergence of equation (5), we easily verify that the divergence-free condition $\nabla \cdot \mathbf{J} = 0$ is automatically enforced. However, this condition is no longer satisfied if the augmented equation (6) is used. Thus, to maintain a divergence-free current density, the auxiliary equation

$$\nabla \cdot [i\omega\mu_0\sigma(\mathbf{A} + \nabla\Psi)] = 0 \tag{8}$$

must be solved simultaneously with the Helmholtz equation. Equations (7) and (8) are valid inside the solution domain Ω and constitute the incompletely gauged $(\mathbf{A}, \Psi)$ coupled vector-scalar potential formulation of Maxwell's equations. In deriving equation (8), we assume $\nabla \cdot \mathbf{J}_S = 0$, which is valid for an inductively coupled source. For directly coupled sources, such as an electric dipole, this is invalid.

By themselves, equations (7) and (8) are insufficient to guarantee a unique vector potential $\mathbf{A}$. The possibility for generation of spurious modes still exists. To remove this possibility, the Coulomb gauge condition $\nabla \cdot \mathbf{A} = 0$ must be applied throughout the solution domain Ω. Following Biro and Preis (1989), we take the divergence of equation (6) to obtain

$$\nabla^2(\nabla \cdot \mathbf{A}) = 0, \tag{9}$$

which shows that the divergence of the vector potential $\mathbf{A}$ satisfies Laplace's equation everywhere inside the solution domain Ω. Thus, to apply the Coulomb gauge, we enforce a zero Dirichlet condition on $\nabla \cdot \mathbf{A}$ along the boundary Γ of the solution domain. This statement follows from a well-known theorem which states that a function u satisfying Laplace's equation $\nabla^2 u = 0$ on some domain Ω, with homogeneous boundary condition $u = 0$ prescribed along the boundary Γ, is identically zero on that domain.

Secondary potentials

The source often enters directly into the formulation of a CSEM problem through the explicit specification of the source current density $\mathbf{J}_S$ in equation (7). However, when a secondary potential formulation is used to model EM induction, a source of arbitrary shape, complexity, and orientation can be introduced conveniently by defining a set of known, primary EM potentials $(\mathbf{A}_p, \Psi_p)$. The primary potentials normally consist of the analytic expression for induction in a homogeneous formation with $\sigma_p = $ const. or a layered electrical conductivity structure of the form $\sigma_p(z)$. However, the primary potentials could be the response of any heterogeneous conductivity structure $\sigma_p(\mathbf{r})$.

The secondary EM potentials $(\mathbf{A}_s, \Psi_s)$ are defined according to $\mathbf{A} \equiv \mathbf{A}_p + \mathbf{A}_s$ and $\Psi = \Psi_p + \Psi_s$, in terms of which the governing equations (7) and (8) become

$$\nabla^2\mathbf{A}_s + i\omega\mu_0\sigma(\mathbf{A}_s + \nabla\Psi_s) = -i\omega\mu_0\Delta\sigma(\mathbf{A}_p + \nabla\Psi_p), \tag{10}$$

$$\nabla \cdot [i\omega\mu_0\sigma(\mathbf{A}_s + \nabla\Psi_s)] = -\nabla \cdot [i\omega\mu_0\sigma(\mathbf{A}_p + \nabla\Psi_p)], \tag{11}$$

where $\Delta\sigma \equiv \sigma - \sigma_p$ is the difference between the conductivity distribution $\sigma(\mathbf{r})$ whose response is required and the background distribution $\sigma_p(\mathbf{r})$ whose response is already known.

Boundary conditions and primary potentials

Boundary conditions on the EM potentials $(\mathbf{A}_s, \Psi_s)$, which are relevant to the induction logging problem considered here, are relatively straightforward, although for other CSEM applications they can become more involved. In this work, the induction logging problem is formulated using a cylindrical geometry, with the vertical coordinate z oriented positive downward. The transmitter is embedded in an inhomogeneous conductor representing the geological formation and is presumed to be a filamentary current loop of finite radius a located at vertical position $z = z_S$ on the z-axis of the cylindrical solution domain Ω. We consider a horizontal loop, but the algorithm is more general and can handle, for example, tilted loops corresponding to deviated boreholes. The outer curved walls and the top and bottom end caps of Ω constitute the outer boundary Γ. The outer walls and end caps are assumed to be located far enough away from the transmitter so that the EM fields there have a negligible value. In this case, a homogeneous Dirichlet boundary condition

$$(\mathbf{A}_s, \Psi_s) \equiv (\mathbf{0}, 0) \text{ on } \Gamma \tag{12}$$

is valid on the outer boundary Γ.

The primary potentials $(\mathbf{A}_p, \Psi_p)$ are chosen to be the potentials from a horizontal loop source located in a homogeneous formation described by a uniform electrical conductivity $\sigma_p = \sigma_0$. For a horizontal loop transmitter of radius a centered on position $(\rho, z) = (0, z_S)$ and carrying a current I, the primary potentials are given by the Hankel transform

$$\mathbf{A}_p(\mathbf{r}) = A_p(\rho, z)\hat{\phi} = \frac{\mu_0 I a \hat{\phi}}{2} \int_0^\infty \frac{1}{\alpha_0} \exp(-\alpha_0|z - z_S|)$$
$$\times J_1(\lambda a)J_1(\lambda\rho)\lambda \, d\lambda \tag{13}$$

and $\Psi_p \equiv 0$, where $\hat{\phi}$ is the unit vector in the azimuthal direction, $\alpha_0^2 = \lambda^2 - i\mu_0\sigma_p\omega$, and J_1 is the Bessel function of order one. Equation (13) verifies that the divergence of $\mathbf{A}_p$ vanishes, a necessary condition for satisfying the Coulomb gauge condition. All Hankel transforms in this paper are calculated using the digital filter method of Guptasarma and Singh (1997).

The weak boundary value problem

Despite the natural cylindrical geometry for the induction logging problem under consideration, the finite-element analysis is conveniently carried out in Cartesian coordinates. In this frame, the vector Laplacian operator readily decomposes into three scalar Laplacian operators, which eases the calculations required to assemble the finite-element matrix. Thus, the secondary magnetic vector potential $\mathbf{A}_s$ is written as

$$\mathbf{A}_s = A_{sx}\hat{x} + A_{sy}\hat{y} + A_{sz}\hat{z}, \tag{14}$$

whereupon equations (10) and (11) become

$$\nabla^2 A_{sx} + i\omega\mu_0\sigma\left(A_{sx} + \frac{\partial\Psi_s}{\partial x}\right) = -i\omega\mu_0\Delta\sigma A_{px},$$

$$\nabla^2 A_{sy} + i\omega\mu_0\sigma\left(A_{sy} + \frac{\partial\Psi_s}{\partial y}\right) = -i\omega\mu_0\Delta\sigma A_{py},$$

$$\nabla^2 A_{sz} + i\omega\mu_0\sigma\left(A_{sz} + \frac{\partial\Psi_s}{\partial z}\right) = -i\omega\mu_0\Delta\sigma A_{pz}, \quad (15)$$

$$i\omega\mu_0\left(\frac{\partial\sigma A_{sx}}{\partial x} + \frac{\partial\sigma A_{sy}}{\partial y} + \frac{\partial\sigma A_{sz}}{\partial z}\right)$$
$$+ i\omega\mu_0\nabla\cdot[\sigma\nabla\Psi_s] = -i\omega\mu_0\nabla\cdot[\sigma\mathbf{A_p}].$$

The FE analysis of 3-D CSEM induction starts with consideration of the weak formulation (Wait and Mitchell, 1985; Biro and Preis, 1990) of the coupled potential boundary value problem defined by equation (15) subject to boundary condition (12). The weak solution is the set of functions $(A_{sx}, A_{sy}, A_{sz}, \Psi_s)$ which satisfies the volume-integrated equations

$$-(\nabla\eta, \nabla A_{sx})_\Omega + i\omega\mu_0\left(\sigma\eta, A_{sx} + \frac{\partial\Psi_s}{\partial x}\right)_\Omega$$
$$= -i\omega\mu_o(\Delta\sigma\eta, A_{px})_\Omega,$$

$$-(\nabla\eta, \nabla A_{sy})_\Omega + i\omega\mu_0\left(\sigma\eta, A_{sy} + \frac{\partial\Psi_s}{\partial y}\right)_\Omega$$
$$= -i\omega\mu_o(\Delta\sigma\eta, A_{py})_\Omega,$$

$$-(\nabla\eta, \nabla A_{sz})_\Omega + i\omega\mu_0\left(\sigma\eta, A_{sz} + \frac{\partial\Psi_s}{\partial z}\right)_\Omega \quad (16)$$
$$= -i\omega\mu_o(\Delta\sigma\eta, A_{pz})_\Omega,$$

$$i\omega\mu_0\left(\eta, \frac{\partial\sigma A_{sx}}{\partial x} + \frac{\partial\sigma A_{sy}}{\partial y} + \frac{\partial\sigma A_{sz}}{\partial z}\right)_\Omega$$
$$- i\omega\mu_0(\sigma\nabla\eta, \nabla\Psi_s)_\Omega = i\omega\mu_0(\sigma\nabla\eta, \mathbf{A}_p)_\Omega$$

for every suitable choice of the test function $\eta(\mathbf{r})$. In equation (16) and hereafter, the shorthand notation

$$(u, v)_\Omega \equiv \int_\Omega uv\, d\Omega \quad \text{and} \quad (\nabla u, \nabla v)_\Omega \equiv \int_\Omega \nabla u\cdot\nabla v\, d\Omega \quad (17)$$

is used for volume integrals. Equations (16) were formed by multiplying each equation (15) by $\eta(\mathbf{r})$ and then integrating over the solution domain Ω. The test function $\eta(\mathbf{r})$ can be any continuous function that vanishes on the boundary Γ and has square-integrable spatial derivatives.

In the derivation of equation (16), the four terms in equation (15) that contain second-order derivatives were integrated by parts to reduce by one the order of the differentiation. The two integration-by-parts formulas used are Green's formula,

$$(u, \nabla^2 v)_\Omega = -(\nabla u, \nabla v)_\Omega + \text{surface terms}, \quad (18)$$

and a related identity,

$$(u, \nabla\cdot[\sigma\nabla v])_\Omega = -(\sigma\nabla u, \nabla v)_\Omega + \text{surface terms}. \quad (19)$$

Integration by parts is standard practice in FE analysis. Without it, the linear approximation of the vector potential $\mathbf{A_s}$ that we plan to use [see equation (20)] would not make sense. The surface terms appearing in equations (18) and (19), which are 2-D integrals over the boundary Γ, vanish because the test function $\eta(\mathbf{r})$ is zero on the boundary of Ω.

The weak solution, despite its name, is unique (Wait and Mitchell, 1985) and satisfies both the strong formulation of the boundary value problem [equations (10–12)] and the weak formulation, [equation (16)]. The equivalence of the weak and strong solutions is a fundamental property of Euler-type second-order partial differential equations. For a more complete discussion see Silvester and Ferrari (1996). Our central objective is to find the weak solution using a FE approximation.

Finite-element matrix assembly

If piecewise linear expansions are used for the EM potentials $(\mathbf{A_s}, \Psi_s)$, the weak system of differential equations given by equation (16) can be reduced to a sparse system of linear algebraic equations. The latter is readily solved by an iterative sparse matrix routine. To assemble the sparse FE system of equations, the 3-D solution domain Ω is first discretized into a mesh of nonoverlapping polyhedral elements with nodes at the vertices. Later, we discuss the mesh generation algorithm, which partitions the domain Ω into tetrahedra.

To initiate the FE sparse matrix assembly, the EM potentials $(\mathbf{A_s}, \Psi_s)$ are expanded into a piecewise linear representation:

$$\mathbf{A_s}(\mathbf{r}) = \sum_{j=1}^{N} A_{sxj}\alpha_j(\mathbf{r})\hat{x} + A_{syj}\alpha_j(\mathbf{r})\hat{y} + A_{szj}\alpha_j(\mathbf{r})\hat{z}, \quad (20)$$

$$\Psi_s(\mathbf{r}) = \sum_{j=1}^{N} \psi_{sj}\alpha_j(\mathbf{r}), \quad (21)$$

where $\alpha_j(\mathbf{r})$ is a linear nodal basis function (Everett and Schultz, 1996) associated with node j of the mesh, while $(A_{sxj}, A_{syj}, A_{szj}, \psi_{sj})$ for each of $j = 1, \ldots, N$ are unknown coefficients to be found by the FE analysis. There are N nodes in the interior of the mesh, not including the nodes that lie on the boundary Γ. When nodal basis functions are used in the expansions equations (20) and (21), the $4N$ coefficients are equal to the values (as yet unknown) of the secondary EM potentials on the interior nodes of the mesh.

The piecewise linear expansions for the secondary EM potentials, given by equations (20) and (21), are inserted into equation (16). This insertion clearly generates only four equations in the $4N$ unknown coefficients, a grossly underdetermined system. However, a test function $\eta(\mathbf{r})$ has yet to be specified. The test function $\eta(\mathbf{r})$ can be chosen as the nodal basis function $\alpha_i(\mathbf{r})$ associated with an interior node i of the mesh. Indeed, in the Galerkin method a well-determined set of $4N$ linear equations in $4N$ unknowns is generated if each of the N basis functions $\{\alpha_i(\mathbf{r})\}_{i=1}^{N}$ is used, in turn, as the test function. It can be shown (Wait and Mitchell, 1985) that as $N \to \infty$, the unique solution to this well-determined system of equations converges to the strong solution of the boundary value problem prescribed by equations (12) and (15).

The linear system that results from applying the Galerkin method can be written in the form

$$\Lambda\mathbf{u} = \mathbf{b}, \quad (22)$$

where the FE matrix Λ is a $4N \times 4N$ sparse complex block symmetric matrix. Each of the 4×4 submatrices is complex

symmetric. After the linear system equation (22) is solved [using the quasi-minimal residual (QMR) method described in Appendix A], the solution vector **u** contains the calculated secondary EM potentials ($\mathbf{A_s}$, Ψ_s), stored according to $\mathbf{u} = (\mathbf{u}_1, \mathbf{u}_2, \ldots, \mathbf{u}_N)^T$, with

$$\mathbf{u}_i = (A_{sxi}, A_{syi}, A_{szi}, \psi_{si}),^T \quad (23)$$

where $A_{sxi} \equiv A_{sx}(\mathbf{r}_i)$ is the x-component of the secondary vector potential $\mathbf{A_s}$ evaluated at node i of the mesh, and so forth.

The FE block matrix Λ is composed of 4×4 symmetric submatrices, given for each of $i, j = 1, \ldots, N$ by

$$\Lambda_{ij} = \begin{pmatrix} \gamma_{ij} I_{33} & i\omega\mu_0(\sigma\alpha_i, \nabla\alpha_j)_\Omega \\ i\omega\mu_0(\sigma\alpha_i, \nabla\alpha_j)_\Omega^T & -i\omega\mu_0(\sigma\nabla\alpha_i, \nabla\alpha_j)_\Omega \end{pmatrix}. \quad (24)$$

In equation (24), I_{33} is the 3×3 identity matrix and γ_{ij} is the scalar function $\gamma_{ij} \equiv -(\nabla\alpha_i, \nabla\alpha_j)_\Omega + i\omega\mu_0(\sigma\alpha_i, \alpha_j)_\Omega$. The electrical conductivity is assumed constant over each tetrahedron, in which case all the integrals involved in assembling the FE matrix Λ can be calculated analytically.

Vector **b** appearing in equation (22) is of the form $\mathbf{b} = (\mathbf{b}_1, \mathbf{b}_2, \ldots, \mathbf{b}_N)^T$, with

$$\mathbf{b}_i = -i\omega\mu_0 \left[\sum_k A_{pxk}\zeta_{ik}, \quad \sum_k A_{pyk}\zeta_{ik}, \quad \sum_k A_{pzk}\zeta_{ik}, \right.$$
$$\left. - \sum_k (A_{pxk}\theta_{ikx} + A_{pyk}\theta_{iky} + A_{pzk}\theta_{ikz}) \right]^T, \quad (25)$$

where

$$\zeta_{ik} = (\Delta\sigma\alpha_i, \alpha_k)_\Omega, \quad \theta_{ikx} = \left(\sigma\frac{\partial\alpha_i}{\partial x}, \alpha_k\right)_\Omega,$$
$$\theta_{iky} = \left(\sigma\frac{\partial\alpha_i}{\partial y}, \alpha_k\right)_\Omega, \quad \theta_{ikz} = \left(\sigma\frac{\partial\alpha_i}{\partial z}, \alpha_k\right)_\Omega \quad (26)$$

and the summations are over all nodes connected to node i. Vector **b** represents the source contribution to the FE linear system equation (22). The coefficients $(A_{pxk}, A_{pyk}, A_{pzk})$ are prescribed before the calculations begin; for example, $A_{pxk} = A_{px}(\mathbf{r_k})$ is the x-component of the primary EM potential $\mathbf{A}_p$ evaluated at node k of the mesh, where $\mathbf{A}_p$ is given by equation (13). We assume that $\mathbf{A}_p$ varies linearly between mesh vertices.

The FE matrix Λ is sparse because the nodal basis function $\alpha_i(\mathbf{r})$ vanishes outside the tetrahedra containing node i as a vertex, implying that the integrals in equations (24) and (25) are zero if node i is not connected to node j. The sparsity of matrix Λ is therefore determined by the node connectivity map. The sparse system of equation (22) is solved using the QMR method (Freund et al., 1992) with simple Jacobi preconditioning (Newman and Alumbaugh, 1995, 1996) (see Appendix A).

MESH GENERATOR WITH LOCAL REFINEMENT

The 3-D FE analysis of borehole CSEM responses involves finding an approximate solution to the system of differential equations (15) defined on the cylindrical domain Ω. To make this approximation, the EM potentials ($\mathbf{A_s}$, Ψ_s) are expanded in terms of nodal basis functions [equations (20) and (21)], defined with respect to a tetrahedral decomposition of the solution domain Ω. The algorithm used to generate the cylindrical mesh consists of two distinct steps: (a) quasi-uniform tetrahedralization of a solid cylinder and (b) optional local mesh refinement. Each of these steps is discussed below.

Quasi-uniform tetrahedralization of a cylinder

The first step of the mesh generation algorithm is to construct a quasi-uniform tetrahedralization of a solid cylinder of finite radius ρ_{max} and length L. A tetrahedralization is defined as a set of nonoverlapping tetrahedra that fills a specified region of 3-D space, along with a list of coordinates of the tetrahedral vertices and an integer array that lists the four vertices, or nodes, belonging to each tetrahedron. A quasi-uniform cylindrical tetrahedralization is one in which the radial node density is constant thoughout the cylinder and the vertical node density is also constant except where necessary to conform to layering in the geoelectrical structure. The cylinder carries a spatially varying electrical conductivity denoted by $\sigma(\mathbf{r})$, which reflects the geology of the formation under study.

Our quasi-uniform tetrahedralization of a cylinder generates tetrahedra, as described below, that are well shaped (no long, thin ones to degrade the accuracy of the FE approximation). The azimuthal distribution of nodes is uniform. The approach is essentially a deterministic packing of tetrahedra into a cylinder. Alternative 3-D mesh generation schemes based on Delaunay tetrahedralizations (Joe, 1991) of randomly or pseudo-randomly generated point sets are not considered here because they could generate poorly shaped tetrahedra.

The integrity of an individual tetrahedron is conveniently measured by its quality factor Q (Liu and Joe, 1996), which is given by the formula

$$Q = 12(3V)^{2/3} \left\{ \sum_{i \neq j}^4 L_{ij}^2 \right\}^{-1}. \quad (27)$$

In equation (27), V is the volume of the tetrahedron and L_{ij} is the length of the edge connecting vertices i and j. The quality factor ranges from $Q = 0$ for poorly shaped or long, thin tetrahedra to $Q = 1$ for well-shaped or regular tetrahedra. In practice, high-quality meshes exhibit a quality-factor distribution that peaks near $Q \sim 0.8$, with few if any tetrahedra falling below $Q \sim 0.6$.

The procedure for decomposing the solid cylinder into high-quality, nonoverlapping tetrahedra begins by triangulating a single horizontal disk, using the series of refinements outlined in Figure 1. Once the disk is triangulated to the required level of refinement, tetrahedralization of the cylinder proceeds with a vertical stacking of a number of triangulated disks. Corresponding nodes on vertically adjacent disks are connected so that prisms with two triangular base planes and three quadrilateral sides are formed. These pentahedra are readily decomposed into three subtetrahedra. The uniform cylindrical tetrahedralization is complete once all the pentahedra are decomposed into their three constituent subtetrahedra. The number and vertical separation of triangulated disks, in addition to the cylinder aspect ratio $\alpha = \rho_{max}/L$, are adjustable parameters that can be tuned to optimize the quality of the mesh and the overall number of constituent tetrahedra. The triangulated disks can be constrained to occupy certain z-positions to accommodate any geoelectrical layering.

Local mesh refinement

Liu and Joe (1996) have published a paper on high-quality local refinement of tetrahedral meshes on which we have based our second step of the mesh generation process. In general, local mesh refinement is used in CSEM modeling to create a fine mesh in regions of the solution domain Ω where the EM field gradients are large, such as near sharp electrical conductivity gradients or discontinuities. Also, a fine mesh might be required in the vicinity of the receiver (RX) to obtain a solution of higher accuracy there. Another approach to adaptive mesh refinement can be found in Travis and Chave (1989).

The first step of the local mesh refinement algorithm is selecting a region S_1 of the cylinder to be refined. The selection of S_1 is done manually so that heterogeneities which generate steep gradients in the secondary field are more finely discretized. Once S_1 is selected, all tetrahedra inside S_1 are identified and marked for refinement. New nodes, termed split points, are then placed at the midpoints of each of the six edges of every marked tetrahedron. Obviously, two adjacent marked tetrahedra will share a certain number of split points: exactly one if they are joined by an edge or exactly three if they are joined by a facet. Each marked tetrahedron, along with its six newly acquired split points, is then decomposed into eight good-quality subtetrahedra by using the SUB_8 refinement scheme shown in Figure 2.

The mesh that results using only SUB_8 refinement of the marked tetrahedra is unacceptable for FE analysis because the unmarked tetrahedra that share an edge or a facet with a marked tetrahedron have inherited exactly one or exactly three split points, respectively. These tetrahedra are improperly formed because they have one or more extra nodes that
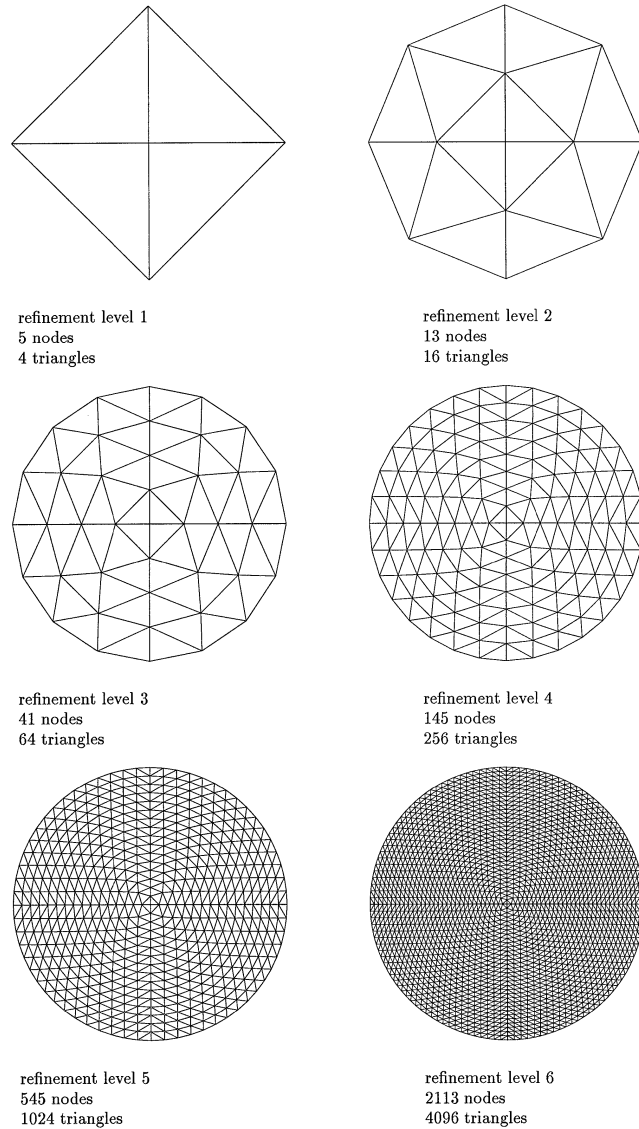

FIG. 1. Various refinement levels of the 2-D disk triangulation procedure. Refinement level 1 (top left) consists of five nodes and four triangles. Refinement level 2 (top right) is formed by subdividing each of the triangles of refinement level 1 into three smaller triangles. Refinement level 2 is completed by an arc adjustment procedure, in which those new nodes situated on a chord connecting two old nodes are projected outward to the chord radius along a ray emanating from the origin. All subsequent refinement levels are constructed in this manner. Once the refinement level is specified, the solid cylindrical mesh is constructed by vertical stacking of a number of these disks along the axis of the cylinder. Nodes on adjacent disks are joined by vertical edges to form triangular prisms, or pentahedra.
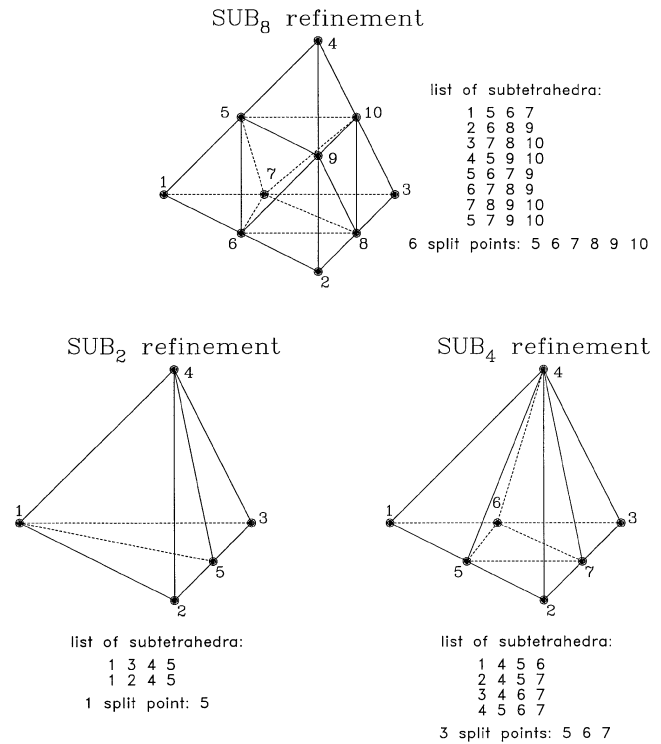

FIG. 2. Decompositions of tetrahedra into two, four, or eight subtetrahedra, depending on the number of split points present [after Liu and Joe (1996)]. The SUB_8 refinement scheme (top) is used to refine marked tetrahedra (see text for definition), which always contain six split points. The SUB_2 (bottom left) and SUB_4 (bottom right) refinement schemes are used to refine improperly formed tetrahedra that contain either one or three split points, respectively.

are not at the vertices. The improperly formed tetrahedra cause the mesh to be defective, leading perhaps to large numerical errors in a FE solution. However, the improperly formed tetrahedra are readily refined (Liu and Joe, 1996) into either two or four high-quality subtetrahedra, according to the number of split points present. The SUB_2 and SUB_4 refinement schemes are shown in Figure 2. Once all the improperly formed tetrahedra are so refined, the mesh is no longer defective and can be used for FE analysis.

In the present implementation of the mesh generator, the refinement region S_1 must be convex, which means that any line segment connecting any two points in S_1 lies wholly inside S_1. If the region S_1 is nonconvex, a tetrahedron could possibly inherit exactly two split points. This case was examined by Liu and Joe (1996) but is problematic and would require a considerable amount of additional computer programming to resolve. The mesh generator exits with a fatal error if a tetrahedron with exactly two split points is detected, and the mesh must be redesigned.

A mesh that has been refined locally according to the above prescription can be further refined. This procedure starts by defining a second refinement region, S_2. The local refinement algorithm we have implemented is quite general: region S_2 can completely enclose region S_1 if required, it can be completely enclosed by region S_1, or the two refinement regions can overlap partially. Indeed, multiple (more than two) nested or disjoint refinement regions are permissible, as long as each refinement region S_i is convex. However, the quality factor Q of SUB_2, SUB_4, and SUB_8 subtetrahedra deteriorate under several refinements. The worsening quality of the mesh determines the practical limit to the number of useful refinements that can be made.

RESULTS

The FE code was checked by computing the CSEM responses of several 1-D, 2-D, and 3-D geoelectrical models. The FE-computed responses are compared in this section to equivalent responses computed using other solution techniques.

1-D modeling: FE versus analytic

The FE code was first tested against the analytic solution for a two-layer geoelectrical structure having an electrical conductivity profile

$$\sigma(z) = \begin{cases} \sigma_1 & z < 0 \\ \sigma_0 & z > 0 \end{cases} \tag{28}$$

corresponding to two semi-infinite homogeneous beds with the bed interface at $z = 0$. The transmitter loop is located on the z-axis, or $\rho = 0$, at a distance $z_S > 0$ beneath the interface. The vertical magnetic field along the z-axis is given analytically (Nabighian, 1988) by

$$H_z(z) = I a \int_0^\infty \frac{\lambda^2 \exp(\alpha_1 z - \alpha_0 z_S)}{\alpha_0 + \alpha_1} J_1(\lambda a)\, d\lambda \quad z \leq 0, \tag{29}$$

$$H_z(z) = \frac{Ia}{2} \int_0^\infty \frac{\lambda^2}{\alpha_0} [\exp(-\alpha_0 |z - z_S|) + R \exp[-\alpha_0(z + z_S)] J_1(\lambda a)\, d\lambda, \quad z \geq 0, \tag{30}$$

where $\alpha_j^2 = \lambda^2 - i \mu_0 \omega \sigma_j$ for $j = 0, 1$ and

$$R \equiv \frac{\alpha_0 - \alpha_1}{\alpha_0 + \alpha_1} \tag{31}$$

is the reflection coefficient.

The secondary vertical magnetic field $H_{sz}(z)$ is defined as the difference between the total field component given by equations (29) and (30) and the primary field component $H_{pz}(z)$ from the same excitation of a homogeneous formation of electrical conductivity σ_0. The primary component $H_{pz}(z)$ is obtained either by setting $\sigma_1 = \sigma_0$ in equations (29) and (30) or alternatively by taking the z-component of the curl of equation (13) and dividing by μ_0. The secondary vertical magnetic field in either case is

$$H_{sz}(z) = \frac{Ia}{2} \int_0^\infty \frac{\lambda^2}{\alpha_0} \exp(-\alpha_0 z_S)[T \exp(\alpha_1 z) - \exp(\alpha_0 z)] J_1(\lambda a)\, d\lambda \quad z \leq 0, \tag{32}$$

$$H_{sz}(z) = \frac{Ia}{2} \int_0^\infty \frac{\lambda^2}{\alpha_0} R \exp[-\alpha_0(z + z_S)] J_1(\lambda a)\, d\lambda, \quad z \geq 0, \tag{33}$$

where $T \equiv 1 + R$.

Figures 3–5 compare the analytic solution given by equations (32) and (33) against equivalent finite-element numerical results for three different conductivity contrasts: $\sigma_1/\sigma_0 = 10$, 100, and 10^5. In all three cases the lower half-space conductivity is $\sigma_0 = 0.1$ S/m. Conductivity contrasts of these magnitudes are often encountered during petroleum well logging, although in such cases σ_0 is normally lower than 0.1 S/m.

The FE code computed the secondary EM potentials $(\mathbf{A}_s, \Psi_s)$ which were then postprocessed into the format $H_{sz}(z)$ using the moving least-squares interpolation (MLSI) algorithm described in Appendix B. The complex analytic solutions are represented in the figures by the solid (real part) and dashed (imaginary part) curves, while the circles correspond to the FE/MLSI solutions computed on a mesh with four nested local refinements in the vicinity of the interface $z = 0$. To demonstrate the effectiveness of the local mesh refinement, the FE/MLSI solutions without any local refinement (calculations were made at refinement level 6; see Figure 1) are shown by the triangles. These solutions clearly exhibit poor agreement with the analytic solution. The excellent performance of the FE/MLSI code with local mesh refinement, particularly for the high-contrast model ($\sigma_1/\sigma_0 = 10^5$), is the result of preconditioning of the sparse linear system. Preconditioning improves the matrix condition number and enables convergence of the iterative QMR solver for very high-contrast electrical models. However, the QMR solver can diverge for high-contrast models if preconditioning is not used. Convergence is achieved in about 300–800 iterations, and the CPU time is between 40 minutes to 2 hours on an SGI Origin 200 workstation with 512 Mb of RAM.

2-D modeling: FE versus hybrid code

The case of a vertical borehole embedded in a double half-space formation was considered as a 2-D axisymmetric test problem. Figure 6 shows the problem geometry. The volume $\rho \leq \rho_{bh}$ could represent a vertical, conductive mud-filled borehole or fluid invasion zone. The two semi-infinite beds have

contrasting electrical conductivities given by σ_0 and σ_1, respectively. The EM fields are generated by an oscillating current loop of radius a and frequency ω placed at a distance z_S below the interface $z = 0$.

The problem is two dimensional because the geoelectrical structure is axially symmetric, i.e., $\sigma = \sigma(\rho, z)$. The borehole in this case behaves like an open waveguide structure, so that a mode spectrum can be defined as consisting of a discrete part in the radial direction in addition to a continuum in the vertical direction. Chew et al. (1984) present a semianalytic mode matching, or hybrid, method for approximating the mode spectrum and hence determining the EM response of axially symmetric structures.

The FE/MLSI-computed solution for the secondary vertical magnetic field $H_{sz}(z)$ along the symmetry axis is compared to the equivalent mode-matching semianalytic solution. The solid and dashed lines in Figure 7 correspond to the complex mode-matching solution. The circles correspond to the FE/MLSI solution computed on a mesh containing six nested

FIG. 4. Same as Figure 3 except for a conductivity contrast of 100.
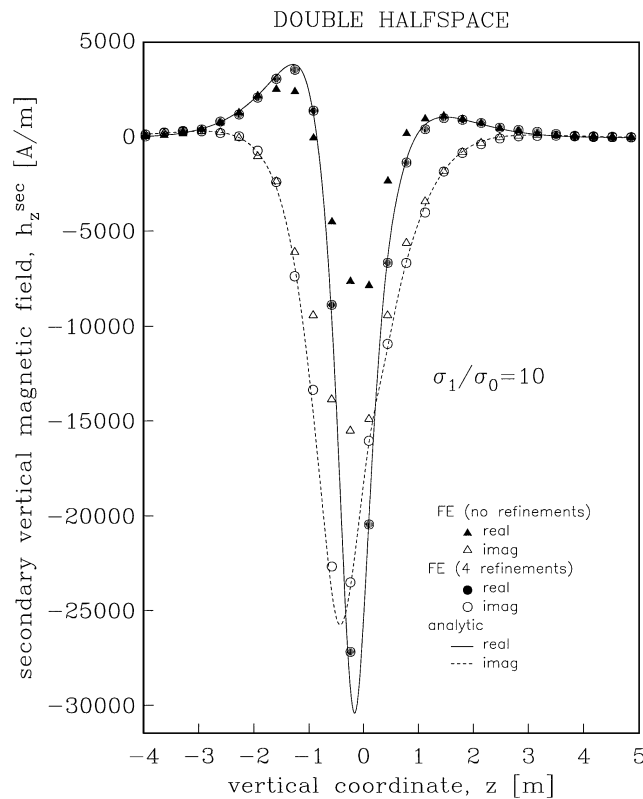

FIG. 3. A comparison of the finite-element solution against the analytic one for the two-layer geoelectric model. The field is caused by a finite-loop horizontal transmitter of radius $a = 0.01$ m carrying a current of 10^{10} Å oscillating at 2.5 MHz. The solution is linear in terms of the *TX* current, so any value chosen will only scale the numerical result. The loop is placed at $z_s = 1.5$ m below the interface. The cylindrical domain over which the FE response was performed has a radius $\rho_{max} = 9$ m and length $L = 20.35$ m. The skin depth in the lower half-space is about 1 m. The conductivity contrast is 10. The first mesh refinement was made in the region $0 \leq \rho \leq 4.0$ m and $-4.0 \leq z \leq 4.0$ m. This region was subsequently reduced during the remaining three nested local refinements. The final mesh refinement region was $0 \leq \rho \leq 0.5$ m and $-1.0 \leq z \leq 1.0$ m.
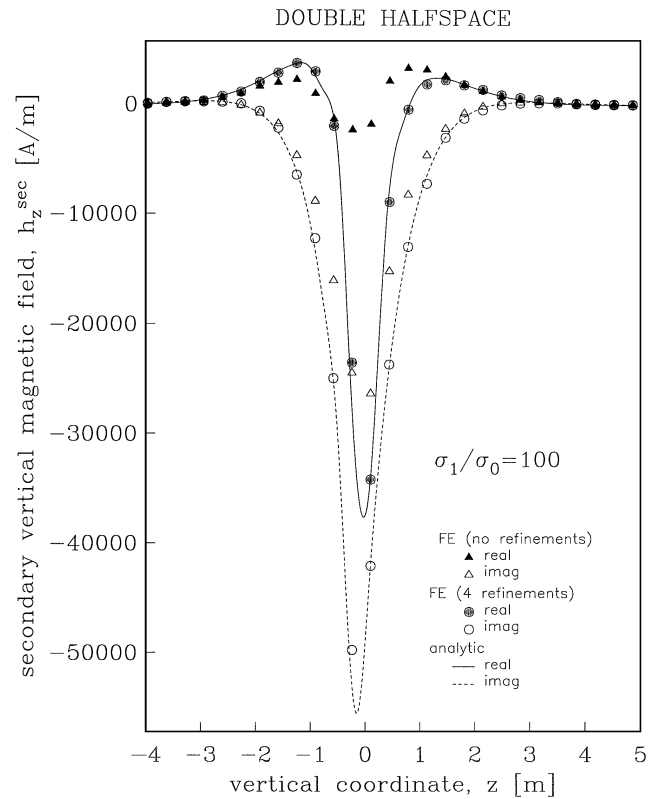

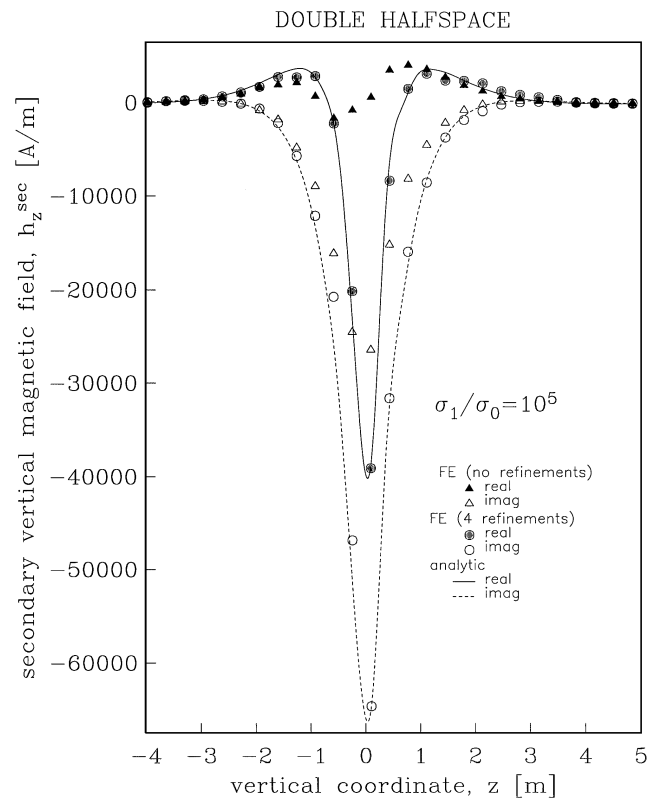FIG. 5. Same as Figure 3 except for a conductivity contrast of 10^5.

local refinements in the vicinity of the interface $z = 0$. The agreement is very good. The FE/MLSI solution without any local mesh refinement (refinement level 6) is shown by the triangles; it is in poor agreement with the hybrid solution.

The FE-computed responses are relatively insensitive to the choice of the whole-space electrical conductivity σ_p used in equation (13) to generate the primary vector potential $\mathbf{A}_p$. Figure 8 uses three different choices for the primary conductivity to illustrate FE/MLSI-computed responses for the axially symmetric model shown in Figure 6. In the figure, the CSEM response is plotted using three different primary vector potentials, each of the form of equation (13) but with different σ_p values. All three results indicate very good agreement with the hybrid solution. The robustness of the FE solutions with respect to the choice of σ_p contrasts with certain other methods, such as the successive approximation technique of Zhang and Zhang (1998), which imposes restrictions on the selection of σ_p to achieve convergence.

3-D modeling: FE versus FD

The performance of the FE code was also tested for a fully 3-D problem. The geometry is shown in Figure 9 and consists of a conductive 90° sector of $\sigma_1 = 1$ S/m placed in a homogeneous formation characterized by $\sigma_0 = 0.1$ S/m. The conducting sector eliminates any axial symmetry and enforces electric currents to flow in the vertical, azimuthal, and radial directions. The primary conductivity is assigned as $\sigma_p = \sigma_0$ so that the conducting sector acts as a spatially distributed current source for the secondary EM potentials. As before, the primary source is the transmitting coil, which is placed at $z_S = 1.5$ m on the z-axis and is energized by a 2.5-MHz ac current of 10^{10} A.

The accuracy of the $(\mathbf{A}_s, \Psi_s)$ FE analysis depends strongly on mesh size and quality. Therefore, careful attention must be paid to the mesh design to achieve good results with reasonable computational effort. Because the conducting sector behaves like a secondary current source, sharp gradients in EM fields are expected near its boundaries. Consequently, our efforts at local mesh refinement were focused in that region. Figure 10 shows vertical and horizontal projections of a small but otherwise typical mesh containing two local refinements. The coarse mesh has the same basic topology but contains far fewer nodes than the fine mesh with three local refinements, which was eventually used to generate accurate EM responses.

The FE/MLSI-computed responses for the 3-D sector model are compared against those computed by a FD method (Newman and Alumbaugh, 1995). Figure 11 shows the results
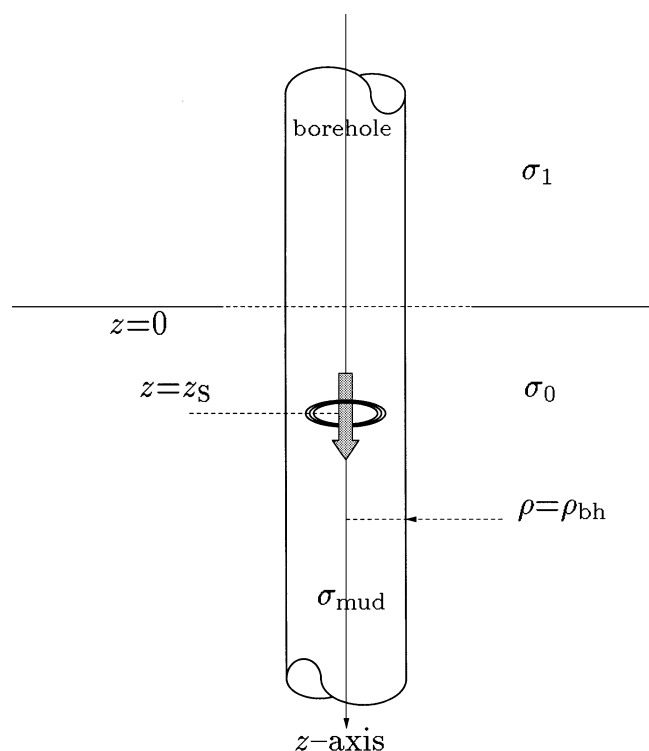

FIG. 6. The axisymmetric geoelectrical model of a borehole embedded in two semi-infinite beds. The electrical conductivity of the upper bed is $\sigma_1 = 1$ S/m, while that of the lower bed is $\sigma_0 = 0.1$ S/m. The axial loop transmitter is located at $z_s = 1.5$ m below the interface at $z = 0.0$. The borehole radius is $\rho_{bh} = 0.5625$ m, which is unrealistically large, but this is just a test problem used for validating the algorithm. The ac driving current has a frequency of 500 kHz and an amplitude of 10^{10} Å. The borehole is assumed to be filled with conductive mud of electrical conductivity $\sigma_{\text{mud}} = 3$ S/m.
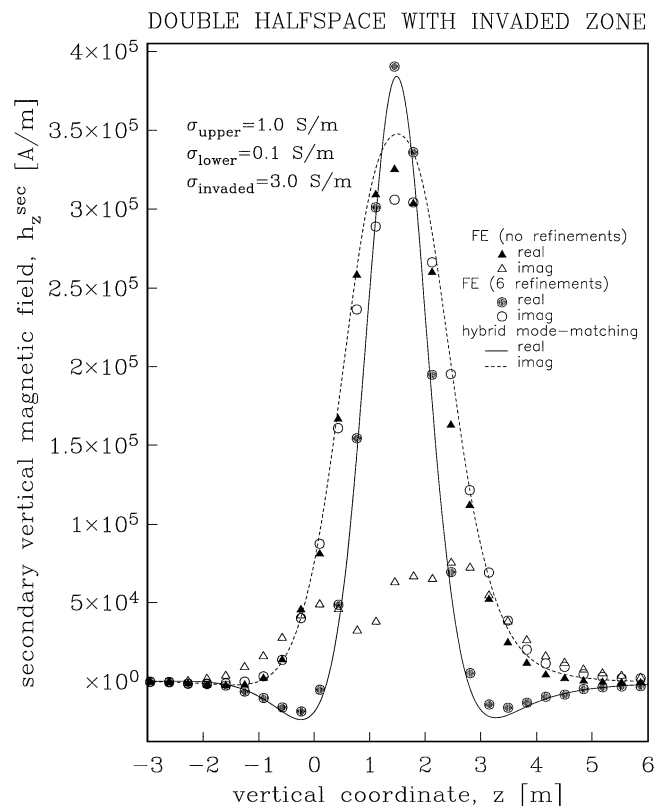

FIG. 7. A comparison of the FE/MLSI-computed solution (circles) with six local mesh refinements and the hybrid mode-matching solution (solid and dashed lines) for the 2-D axisymmetric problem shown in Figure 6. The FE/MLSI-computed solution (triangles) without any local refinement behaves poorly. In this example, the primary EM potential $\mathbf{A}_p$ is defined for a homogeneous whole-space formation described by $\sigma_p = \sigma_{\text{mud}}$. The field along the z-axis is shown.
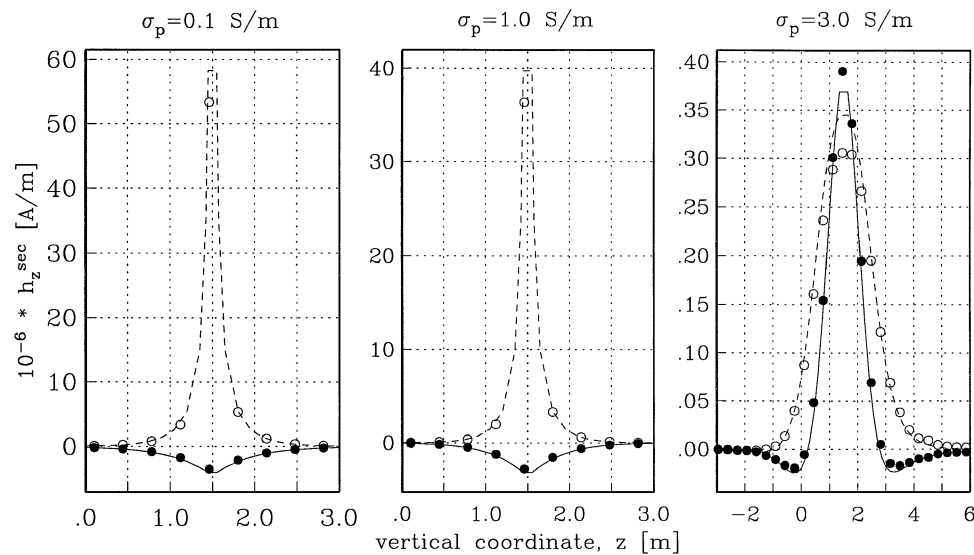
FIG. 8. The sensitivity of the finite-element-computed responses (symbols) to the choice of primary whole-space electrical conductivity σ_p for the axisymmetric model. Very good agreement is obtained in all cases with the hybrid-computed solutions (curves.)
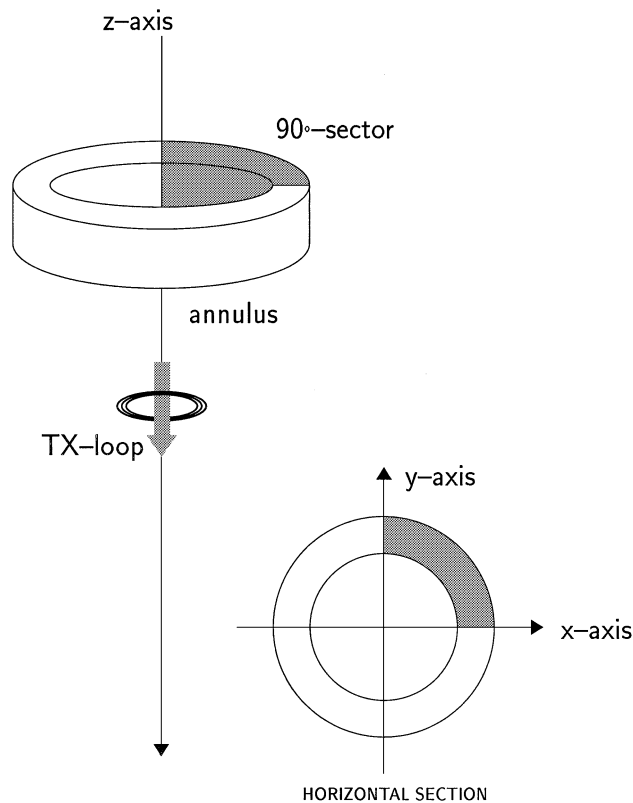

FIG. 9. Geometry of the 3-D test problem. The loop is positioned at $z_s = 1.5$ m, has a radius $a = 0.01$ m, and is fed by a 10^{10}-Å current at a frequency of 2.5 MHz. The loop excites the conducting 90° sector (shaded.) The inner radius, outer radius, and height of the sector are 2.25, 2.8125, and 1.078125 m, respectively. The sector is centered on $z = 0$. The background formation conductivity is $\sigma_0 = 0.1$ S/m, while the conductivity of the sector is $\sigma_1 = 1.0$ S/m. The skin depth in the background medium is $\sim$1.0 m.

for both $H_{sz}(\phi)$ and $E_{s\phi}(\phi)$ along an azimuthal path passing through the center of the sector. The shapes of the response curves make sense on physical grounds. For example, if the sector is replaced by a full 360° annulus excited by the same horizontal loop transmitter, symmetry arguments imply that the direction of the induced eddy currents is strictly azimuthal. However, when the 90° sector is considered, the induced eddy currents retain a strong azimuthal component in the interior of the sector, in addition to a vertical component. This is shown in Figure 11 by the almost constant values of both $H_{sz}(\phi)$ and $E_{s\phi}(\phi)$ for $0 < \phi < \pi/2$. The azimuthal discontinuity of the electrical conductivity in regions close to the edges of the sector forces eddy currents to flow into the radial and vertical directions. Consequently, apart from these edge effects, there should be a reduced signal over the full range of azimuths outside of the sector. This lack of signal can be observed in Figure 11 by the small values of the secondary EM fields over the range $\pi/2 < \phi < 2\pi$. The discrepancies between the FE and the FD responses may be from differences in the underlying numerical algorithms. The FD response averages the **E** field across the boundary of the sector; therefore, we should expect some differences between the two numerical methods. The secondary field is plotted in the figure because it better reveals the underlying physics of the induction process rather than the total field, which is dominated by the primary component.

3-D modeling: Logging format

A practical 3-D problem of interest to the petroleum logging industry was considered. The conductivity model, shown in Figure 12, includes a borehole, fluid invasion zones, and three parallel dipping (tilting) beds. The outer beds are semi-infinite. A compensated logging tool formed by one *TX* loop and two in-line *RX* loops (see Figure 13) was modeled. The tool output is expressed in terms of apparent resistivity, which is a function of the *RX*-induced voltages (Moran and Kunz, 1962). The tool descends within the borehole, and apparent resistivity is

displayed as a function of true vertical depth in Figure 14. For zero dip, the FE-computed induction log compares very well against the same log computed using the 2-D mode-matching method (Chew et al., 1984). For the nonzero tilt cases, a coordinate transformation is performed so that the tetrahedra of the finite-element mesh conform to the dipping bed boundaries. The FE-computed logs are presented for tilt angles of 30°, 45°, and 60° from the horizontal.

DISCUSSION

We introduce the $(\mathbf{A}_s, \Psi_s)$ formulation of CSEM induction for geophysical prospecting applications and develop a 3-D numerical solution using the FE method. Good agreement has been found between the FE-computed responses and certain 1-D analytical, 2-D hybrid, and 3-D FD finite-loop responses of simple geoelectrical models.

Realistic EM induction problems are three dimensional in nature, largely because of the complexity of subsurface geology. In induction logging applications, causes of three dimensionality include a tilting or deviating borehole, washouts, dipping beds, and heterogeneous fluid invasion zones. Thus, modeling of 3-D effects is fundamental for accurate quantitative interpretation of wireline induction and measurement-while-drilling (MWD) logs (Anderson et al., 1996). The FE algorithm we describe, with certain modifications, can be adapted to handle all these problems.

Another important complication is the occurrence of anisotropic electrical conductivity because of cross-bedded and vertically stratified formations. This issue can be addressed using the existing FE code with the inclusion of a conductivity tensor in the governing FE equations, which is not difficult to implement and requires no specialized programming techniques. Also, the performance of the FE code should be tested for a range of frequencies on a single mesh. This will be addressed in a future publication.

Finally, with attention to improving the efficiency, the FE code could further serve as the forward driving module inside a larger software package for multidimensional inversion of different types of CSEM data, including induction and MWD logs.
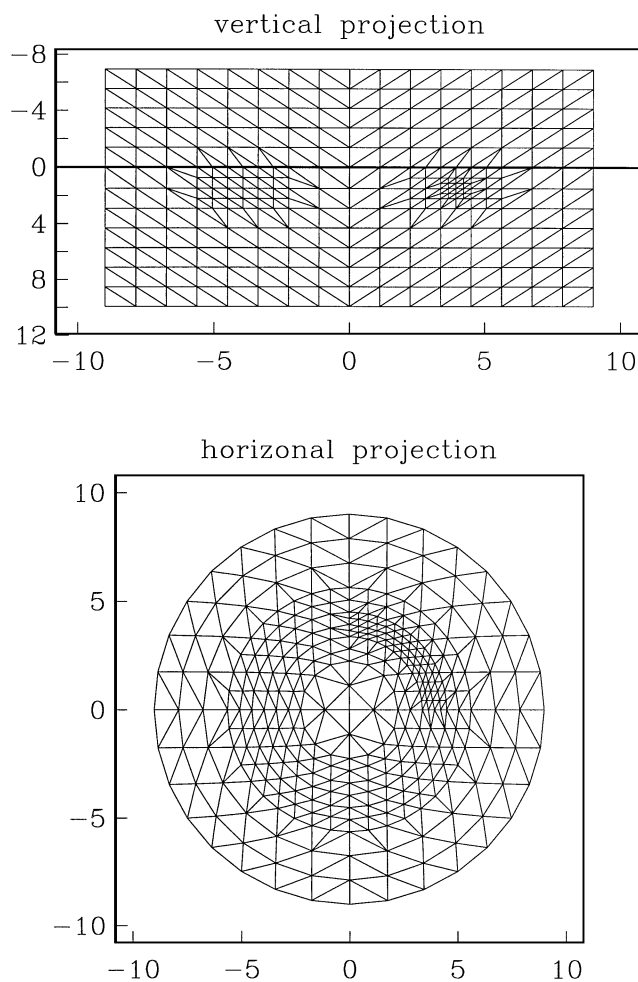

FIG. 10. Horizontal cross-section of a small but otherwise typical finite-element mesh for the plane $z = 0$ passing through the center of a conducting sector like that shown in Figure 9, along with a typical vertical cross-section of the same mesh. The mesh has been locally refined twice in the vicinity of the conducting sector, which in this case is centered just below $z = 0$. Triangular facets of SUB$_2$ and SUB$_4$ subtetrahedra can be seen in both views, bordering the refinement regions. The mesh does not have to be refined in the vicinity of the *TX* because only secondary fields are being computed.
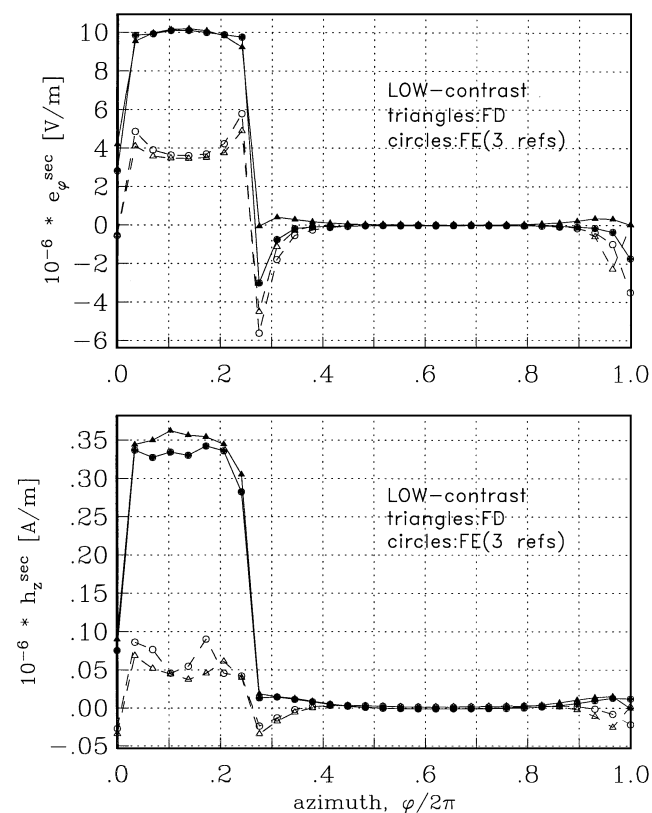

FIG. 11. The secondary vertical magnetic field $H_{sz}(\phi)$, and secondary azimuthal electric field $E_{s\phi}(\phi)$ responses computed using the FE/MLSI (circles) and Sandia FD (triangles) methods along an azimuthal path passing through the center of the conducting sector, i.e., ($\rho = 2.53$ m; $0 \le \phi \le 2\pi$; $z = 0$). Lines are drawn through the symbols for clarity. Dark symbols correspond to the real component, while open symbols correspond to the imaginary component.
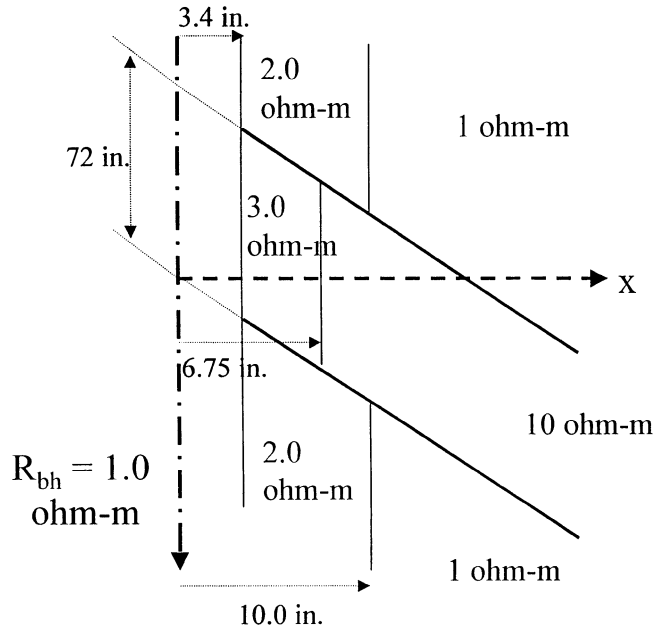
FIG. 12. The geoelectrical structure used for the logging format example. A borehole of radius 3.4 inches (8.6 cm) and conductivity of 1.0 S/m (e.g., resistivity of 1.0 ohm-m) intersects a three-layer formation. The two outer beds are semi-infinite and have a conductivity of 1.0 S/m. The middle bed is more resistive, with a conductivity of 0.1 S/m, and is 72 inches (1.82 m) thick. Fluid-invaded zones are present in the model. For the outer beds, the invaded-zone conductivity is 0.5 S/m and 10.0 inches (25 cm) thick. For the middle bed, these values are 0.333 S/m and 6.75 inches (17.1 cm).
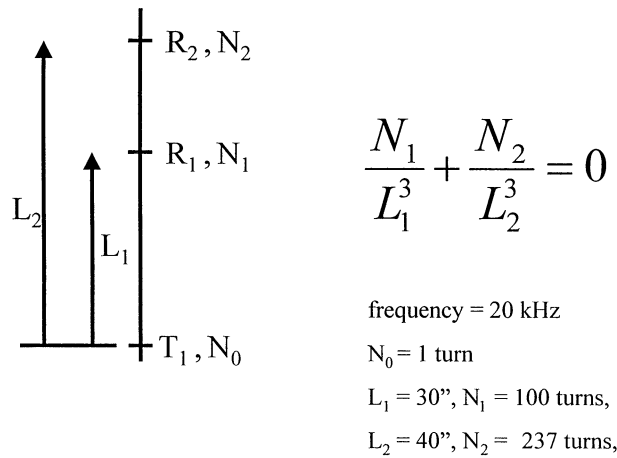

$$\frac{N_1}{L_1^3} + \frac{N_2}{L_2^3} = 0$$

frequency = 20 kHz

N_0 = 1 turn

L_1 = 30", N_1 = 100 turns,

L_2 = 40", N_2 = 237 turns,

FIG. 13. The compensated logging tool, consisting of one loop transmitter (T_1) of $N_0 = 1$ turn oscillating at 20 kHz and two oppositely wound receivers (R_1 and R_2) with $N_1 = 100$ turns and $N_2 = -237$ turns, respectively. The receivers are so configured to cancel the primary component of mutual coupling. The equation at the right of the figure is the condition for tool compensation. Receiver R_1 is located 30 inches (76 cm) above the transmitter, while R_2 is located 40 inches (102 cm) above the transmitter. The tool center is the midpoint between the two receivers.
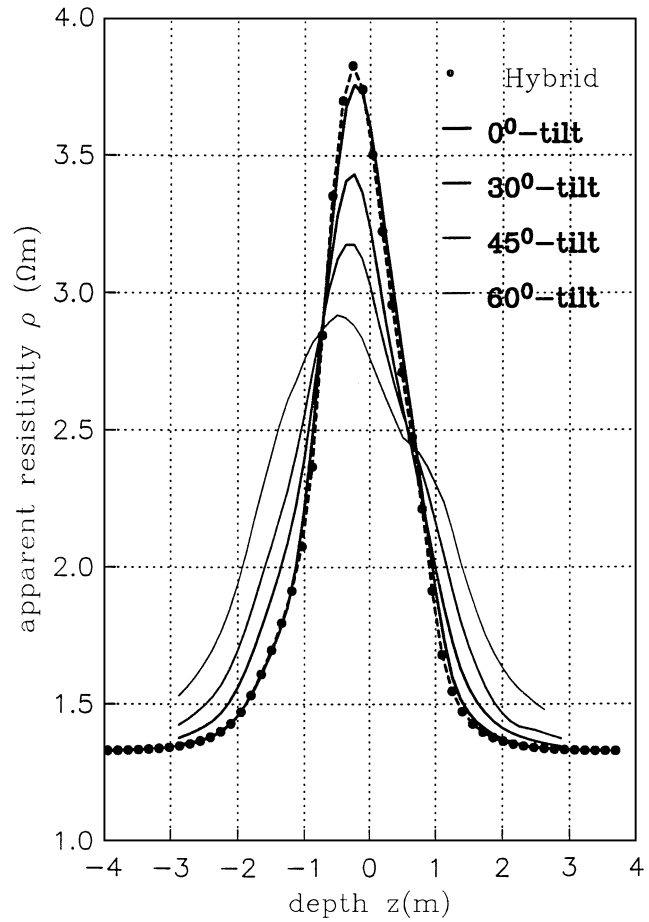

FIG. 14. The computed induction log corresponding to the geoelectric formation shown in Figure 12, as sensed by the compensating logging tool described in Figure 13. The apparent resistivity is evaluated at the tool center as the tool descends down the borehole. Four different dip (tilt) angles were considered. The FE-computed logs are shown by the solid lines. For the zero tilt case, a log computed using the 2-D mode-matching (hybrid) method is shown by the dashed curve with symbols.

REFERENCES

Anderson, B., Barber, T., Druskin, V., Lee, P., Dussan, E., Knizhnermann, L., and Davydycheva, S., 1996, The response of multiarray induction tools in highly dipping formations with invasion and in arbitrary 3-D geometries: 37th Ann. Logging Symp., SPWLA, Paper A, 1–14.

Avdeev, D. B., Kuvshinov, A. V., Pankratov, O. V., and Newman, G. A., 1997, High performance three dimensional electromagnetic modeling using modified Neumann series: Wide band numerical solution and examples: J. Geomag. Geoelectr., **49**, 1519–1539.

Barton, M. L., and Cendes, Z. J., 1987, New vector finite elements for three-dimensional magnetic field computation: J. Appl. Phys., **61**, 3919–3921.

Biro, O., and Preis, K., 1989, On the use of the magnetic vector potential in the finite element analysis of three-dimensional eddy currents: IEEE Trans. Magn., **25**, 3145–3159.

———— 1990, Finite element analysis of 3-D eddy currents: IEEE Trans. Magn., **26**, 418–423.

Boyse, W. E., Lynch, D. R., Paulsen, K. D., and Minerbo, G. N., 1992,

Nodal-based finite element modeling of Maxwell's equations: IEEE Trans. Ant. Propag., **40**, 642–651.

Chang, S. K., and Anderson, B., 1984, Simulation of induction logging by the finite-element method: Geophysics, **49**, 1943–1958.

Chew, W. C., Barone, S., Anderson, B., and Hennessy, C., 1984, Diffraction of axisymmetric waves in a borehole by bed boundary discontinuities: Geophysics, **49**, 1586–1595.

Doll, H. G., 1949, Introduction to induction logging and application to logging wells with oil-based mud: Trans. AIME, **186**, 148–162.

Druskin, V., and Knizhnermann, L., 1994, Spectral approach to solving three-dimensional Maxwell's diffusion equations in the time and frequency domains: Radio Sci., **29**, 937–953.

Everett, M. E., and Schultz, A., 1996, Geomagnetic induction in a heterogeneous sphere: Azimuthally symmetric test computations and the response of an undulating 660-km discontinuity: J. Geophys. Res., **101**, 2765–2783.

Freund, R. W., Golub, G. H., and Nachtigal, N. M., 1992, Iterative solutions of linear systems, *in* Iserles, A., Ed., Acta Numerica 1992: Cambridge Univ. Press, 57–100.

Golub, G. H., and van Loan, C. F., 1996, Matrix computations, 3rd ed.: Johns Hopkins Univ. Press.

Guptasarma, D., and Singh, B., 1997, New digital filters for Hankel transform J_0 and J_1 transforms: Geophys. Prosp., **45**, 745–762.

Joe, B., 1991, Geompack: A software package for the generation of meshes using geometric algorithms: Adv. Eng. Software Workstations, **13**, 325–331.

Kaufman, A. A., and Keller, G. V., 1989, Induction logging: Elsevier Science Publ. Co., Inc.

Lanczos, C., 1958, Linear systems in self-adjoint form: Am. Math. Month., **65**, 665–679.

Liu, A., and Joe, B., 1996, Quality local refinement of tetrahedral meshes based on 8-subtetrahedron subdivision: Math. of Comp., **65**, 1183–1200.

Moran, J. H., and Kunz, K. S., 1962, Basic theory of induction logging and application to study two coil sondes: Geophysics, **27**, 829–858.

Mur, G., 1993, The finite-element modeling of three-dimensional electromagnetic fields using edge and nodal elements: IEEE Trans. Ant. Propag., **41**, 948–953.

Nabighian, M. N., Ed., 1988, Electromagnetic methods in applied geophysics **1**, theory: Soc. Expl. Geophys.

——— 1991, Electromagnetic methods in applied geophysics **2**, applications: Soc. Expl. Geophys.

Newman, G. A., and Alumbaugh, D. L., 1995, Frequency-domain modelling of airborne electromagnetic responses using staggered finite differences: Geophys. Prosp., **43**, 1021–1042.

——— 1996, three-dimensional electromagnetic modeling and inversion on massively parallel computers: Sandia Nat. Lab. Report SAND96-0582.

Omeragic, D., and Silvester, P. P., 1996, Numerical differentiation in magnetic field postprocessing: Internat. J. Num. Mod.: Elect. Net., Dev., Fields, **9**, 99–113.

Paulsen, K. D., and Lynch, D. R., 1991, Elimination of vector parasites in finite element Maxwell solutions: IEEE Trans Micro. Theory Tech., **39**, 395–404.

Silvester, P. P., and Ferrari, R. L., 1996, Finite element methods for electrical engineers: Cambridge Univ. Press.

Smith, J. T., 1996, Conservative modeling of 3-D electromagnetic fields: Geophysics, **61**, 1308–1324.

Sugeng, F., 1998, Modeling the transient EM responses of complex 3-D geological structures using the 3-D full-domain hexahedral edge-element finite-element technique: Presented at the 14th Workshop on Electromagnetic Induction in the Earth, Internat. Assn. Geomagnetism and Aeronomy.

Tabbara, M., Blacker, T., and Belytschko, T., 1994, Finite element derivative recovery by moving least squares interpolants: Comp. Meth. Appl. Mech. Eng., **117**, 211–223.

Travis, B. J., and Chave, A. D., 1989, A moving finite-element method for magnetotelluric modeling: Phys. Earth Planet. Internat., **53**, 432–443.

van den Berg, P. M., and van der Horst, M., 1995, Nonlinear inversion in induction logging using the modified gradient method: Radio Sci., **30**, 1355–1369.

Wait, R., and Mitchell, A. R., 1985, Finite element analysis and applications: John Wiley & Sons, Inc.

Wang, T., and Hohmann, G. W., 1993, A finite-difference time-domain solution for three-dimensional electromagnetic modeling: Geophysics, **58**, 797–809.

Xiong, Z., and Tripp, A. C., 1995, Electromagnetic scattering of large structures in layered earths using integral equations: Radio Sci., **30**, 921–929.

Zanoubi, M. R., Jin, J. M., Donepudi, K. C., and Chew, W. C., 1999, A spectral Lanczos decomposition method for solving 3-D low-frequency electromagnetic diffusion by the finite-element method: IEEE Trans. Ant. Propag., **47**, 242–248.

Zhang, G. J., and Zhang, Z. Q., 1998, Application of successive approximation method to the computation of the Green's function in axisymmetric inhomogeneous media: IEEE Trans. Geosci. and Remote Sens., **36**, 732–737.

Zhdanov, M. S., and Fang, S., 1997, Quasi-linear series in three-dimensional electromagnetic modeling: Radio Sci., **32**, 2167–2188.

APPENDIX A

SPARSE LINEAR ALGEBRAIC SOLVER

The determination of potentials $(\mathbf{A}_s, \Psi_s)$ requires solving equation (22), which is a large, sparse complex symmetric linear system of equations. The quasi-minimal residual (QMR) approach described by Freund et al. (1992) is an iterative procedure designed to solve such problems and has been used in geophysical CSEM modeling by Newman and Alumbaugh (1995, 1996).

The QMR algorithm is based on the concept that a rapidly convergent iterative method for solving equation (22) should try to minimize the residual vector $\mathbf{r}_n \equiv \mathbf{b} - \Lambda \mathbf{u}_n$ at each step of the process. A fundamental study of linear algebra reveals that iterates $\mathbf{u}_n$ which tend to make $\mathbf{r}_n$ small at every step can be constructed from a set of basis vectors $\mathbf{v}_1, \mathbf{v}_2, \ldots, \mathbf{v}_n$ for the nth Krylov subspace $K_n(\mathbf{r}_0, \Lambda)$, where

$$K_n(\mathbf{r}_0, \Lambda) = \mathrm{span}\{\mathbf{r}_0, \Lambda\mathbf{r}_0, \Lambda^2\mathbf{r}_0, \ldots, \Lambda^{n-1}\mathbf{r}_0\}. \quad \text{(A-1)}$$

In equation (A-1), $\mathbf{r}_0 = \mathbf{b} - \Lambda\mathbf{u}_0$ is the residual vector corresponding to an initial guess $\mathbf{u}_0$ for the solution of equation (22). Thus, in the so-called Krylov subspace methods (Golub

and van Loan, 1996), the iterates $\mathbf{u}_n$ will satisfy

$$\mathbf{u}_n = \mathbf{u}_0 + V_n\mathbf{z}_n, \quad \text{(A-2)}$$

where $\mathbf{z}_n$ is a vector of unknown coefficients and

$$V_n \equiv [\mathbf{v}_1 \quad \mathbf{v}_2 \quad \ldots \quad \mathbf{v}_n] \quad \text{(A-3)}$$

is an $N \times n$ rectangular matrix whose columns are the Krylov basis vectors.

The QMR method is a Krylov subspace method in which the basis vectors $\mathbf{v}_1, \mathbf{v}_2, \ldots, \mathbf{v}_n$ at each iteration are generated by a Lanczos-type procedure (Lanczos, 1958). Once the basis vectors for the current iteration are found, the vector $\mathbf{z}_n$ of unknown coefficients is determined by a linear, rank-deficient least-squares analysis designed to make $\mathbf{r}_n$ as small as possible while keeping CPU time and storage requirements low. Refer to Freund et al. (1992) and the references in that paper for complete details about the QMR method. We also implement simple Jacobi preconditioning (Newman and Alumbaugh, 1996) of the finite-element matrix Λ in equation (22) to further enhance the convergence rate of the QMR iterates.

APPENDIX B

MOVING LEAST-SQUARES INTERPOLATION

The physically significant $\mathbf{E_s}$ or $\mathbf{H_s}$ fields must be recovered from the finite-element-computed potentials $(\mathbf{A}_s, \Psi_s)$ by means of numerical differentiation. Several good algorithms exist for this purpose (Omeragic and Silvester, 1996). The problem is not trivial: simple first-order differencing of the nodal potential values is likely to cause serious errors, especially on irregular meshes. We differentiate the FE-computed potentials $(\mathbf{A_s}, \Psi_s)$ using the moving least-squares interpolant (MLSI) scheme originally proposed by Tabbara et al. (1994). In our implementation of this method, each Cartesian component of the vector potential $\mathbf{A}_s$ and the scalar potential Ψ_s are approximated by linear functions of the form $ax + by + cz + d$. The spatial derivatives of the potentials are therefore just the first three coefficients (a, b, c) of the linear function. The MLSI determination of the spatial derivatives of $(\mathbf{A_s}, \Psi_s)$ at an arbitrary test point $\mathbf{r}_t \equiv x_t \hat{x} + y_t \hat{y} + z_t \hat{z}$ in Ω is made in a weighted least-squares sense. Specifically, (a, b, c, d) are found by minimizing the sum of the weighted squared residuals between the linear function and the finite-element-computed values of the EM potentials at the nearest $N \sim 30$ nodes to the test point (see Figure B-1.) The weighting function has a positive exponential form which is maximum at the point $\mathbf{r}_t$ and decreases monotonically with increasing distance away from $\mathbf{r}_t$. The method is called a moving least-squares interpolant because the set of nodal EM potential values used in the least-squares analysis depends on the position of the test point $\mathbf{r}_t$.

At conductivity interfaces, the MLSI method forces a non-physical continuity of the normal component of the electric field. However, for most applications the method works well close to interfaces, as illustrated by the results presented throughout the paper. Other algorithms, such as nodal differentiation, that correctly define the discontinuity in normal electric field may perform better near high-conductivity contrasts.
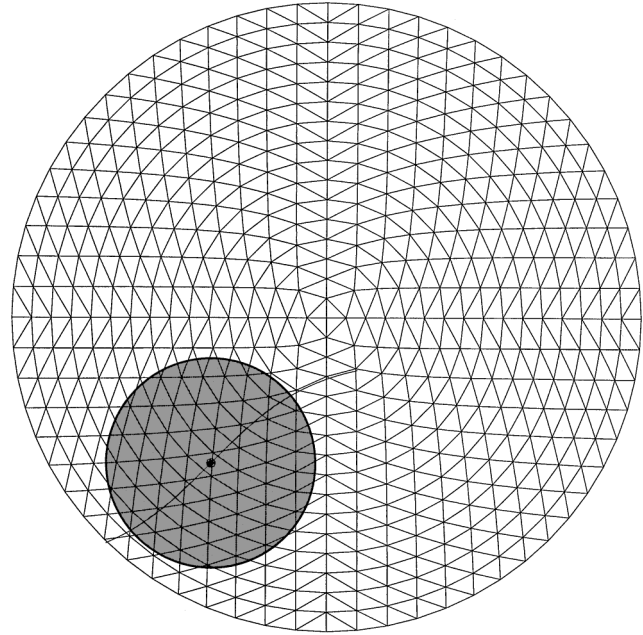

FIG. B-1. The MLSI differentiates the finite-element-computed EM potentials $\mathbf{A}_s, \Psi_s$ to obtain the direct fields $\mathbf{E}$ and $\mathbf{B}$. The spatial derivatives of the potentials are obtained at a given test point $\mathbf{r}_t$ (the solid dot) by fitting a linear function to the FE-computed potential values on the N mesh nodes lying closest to the test point (within the shaded region). The spatial derivatives of the computed EM potentials can be estimated along an arbitrary trajectory, as shown, by moving the test point and the corresponding shaded region along the trajectory. The generalization to three-dimensions is straightforward.